



Auto-ignition during instationary jet evolution of dimethyl ether (DME) in a high-pressure atmosphere

G. Fast^a, D. Kuhn^{a,*}, A.G. Class^a, U. Maas^b

^a Institut für Kern- und Energietechnik, Forschungszentrum Karlsruhe GmbH, Weberstraße 5, D-76133 Karlsruhe, Germany

^b Institut für Technische Thermodynamik, Universität Karlsruhe (TH), Kaiserstraße 12, D-76128 Karlsruhe, Germany

ARTICLE INFO

Article history:

Received 24 January 2008

Received in revised form 12 June 2008

Accepted 16 July 2008

Available online 13 September 2008

Keywords:

Dimethyl ether (DME)

Open jet

Free jet

Instationary flow

Transient jet

High pressure

Low temperature oxidation

Negative temperature coefficient (NTC)

Two stage ignition

Auto-ignition

Particle image velocimetry (PIV)

Laser doppler velocimetry (LDV)

Laser induced fluorescence (LIF)

High-speed shadowgraphy

Ignition delay time

SFB 606

INSFLA

Laminar flame calculation

Probability density function (PDF)

ABSTRACT

The auto-ignition process during transient injection of gaseous dimethyl ether (DME) in a constant high-pressure atmosphere is studied experimentally by laser-optical methods and compared with numerical calculations. With different non-intrusive measurement techniques jet properties and auto-ignition are investigated at high temporal and spatial resolution. The open jet penetrates a constant pressure oxidative atmosphere of up to 4 MPa. During the transient evolution, the fuel jet entrains air at up to 720 K. The subsequent auto-ignition of the ignitable part of the jet occurs simultaneously over a wide spatial extension. The ignition delay times are not affected by variation of the nozzle exit velocity. Thus, the low-temperature oxidation is slow compared with the shorter time scales of mixing, so that chemical kinetics is dominating the process. The typical two-stage ignition is resolved optically with high-speed shadowgraphy at a sampling rate of 10 kHz. The 2D fields of jet velocity and transient mixture fraction are measured phase-coupled with Particle Image Velocimetry (PIV) and Tracer Laser Induced Fluorescence (LIF) during the time-frame of ignition. The instationary Probability Density Functions (PDF) of mixture fraction are described very well by Beta functions within the complete area of the open jet. Additional 1D flamelet simulations of the auto-ignition process are computed with a detailed reaction mechanism for DME [S. Fischer, F. Dryer, H. Curran, *Int. J. Chem. Kinet.* 32 (12) (2000) 713–740; H. Curran, S. Fischer, F. Dryer, *Int. J. Chem. Kinet.* 32 (12) (2000) 741–759]. Calculated ignition delay times are in very good agreement with the measured mean ignition delay times of 3 ms. Supplemental flamelet simulations address the influence of DME and air temperature, pressure and strain. Underneath a critical strain rate the air temperature is identified to be the most sensitive factor on ignition delay time.

© 2008 The Combustion Institute. Published by Elsevier Inc. All rights reserved.

1. Introduction

In the design of new combustion processes for modern internal combustion engines, the mixture formation and subsequent auto-ignition are key factors that influence efficiency and pollutant formation. Nevertheless, the auto-ignition, for example following direct injection in compression-ignition engines, represents a complex phenomenon that is not yet understood completely. In combustion research, different modeling approaches for stationary flames are established for both laminar and turbulent flow fields [3]. During ignition, different time scales in both chemical reactions and turbulent flow complicate a detailed description in technical applications. The auto-ignition of hydrocarbons is initiated by low-temperature oxidation mechanisms that include

temperature-sensitive and fuel-specific reactions [4]. Therefore, ignition delay times have non-linear dependencies on temperature and pressure [5]. With detailed reaction mechanisms the ignition of fuel–air mixtures is predicted very well for simple geometries [6,7]. For more complex geometries reduced mechanisms are often used in Computational Fluid Dynamics (CFD). In turbulent flows, the mass and energy transport across the boundary of a developing ignition zone is influenced by velocity gradients and turbulence. In non-premixed configurations, the chemical kinetics is also coupled to the non-stationary turbulent mixing of fuel and oxidizer. Direct Numerical Simulations (DNS) of initially non-premixed fuel and preheated air predicts auto-ignition at locations with lean mixture compositions [8,9]. This is explained by the dominating influence of air temperature compared with fuel concentration. The increasing delay of auto-ignition with higher scalar dissipation due to increased turbulence is also diagnosed experimentally [10]. This corresponds to the observation that higher ignition tempera-

* Corresponding author.

E-mail address: dietmar.kuhn@kit.edu (D. Kuhn).

Nomenclature

a	strain rate
d	inner nozzle diameter
M	collision molecule
p	pressure
RH	hydrocarbon
t_{ign}	ignition delay time
T	temperature
u	axial velocity component
v	radial velocity component
x/d	distance to nozzle, normalized with diameter d
y	radial coordinate
$y_{0.5u}$	radius at half maximum of the axis mean velocity

x	mole fraction
X	molar mixture fraction

Subscripts

a	condition at jet axis
ch	state of the chamber gas
inj	state of the injection gas
i, j	indexing coordinates
rms	root mean square
0	condition of the injection gas prior to injection
∞	condition of the chamber gas outside the jet

tures are necessary in counter flow configuration of fuel and air when strain rates are raised [11]. The statistical character of turbulence demands models with Probability Density Functions (PDF) of flow properties for the computation of reaction rates and consequently auto-ignition. In recent years, PDF transport equations were developed for different modeling tasks [12–14] and validated by PDF measurements of different scalars and velocity [15,16]. To our knowledge, only few experimental investigations of transient flows with auto-ignition are reported in terms of PDFs [17].

In order to provide a fundamental understanding of individual interacting processes, an idealized injection process is investigated in the present work. The fuel is injected in a gaseous state so that two phase phenomena like spray formation and evaporation are omitted. Instead of a multi-component fuel, a pure combustible substance is used to allow detailed chemical simulations. The investigations should clarify if one of the participating processes is predominant in the auto-ignition during fuel injection under pressures relevant for engines. A further aim is to provide a detailed and accurate data base for the validation of numerical methods that are based on statistical analysis, such as PDFs. Reliable data on instationary PDFs within this jet configuration are available for the first time under high-pressure conditions.

2. Experimental setup

As a model fuel, dimethyl ether (CH_3OCH_3 , DME) is identified from detailed experimental investigations to ensure auto-ignition during the transient jet evolution. The short ignition delay times are represented by higher cetane numbers of DME in comparison with diesel fuel [18,19]. Its thermodynamic properties and critical point (5.264 MPa, 400 K) are comparable to alkanes. In contrast to other ethers, auto-oxidation of DME does not occur and DME does not decompose below 670 K [20]. This is confirmed by detailed chemical simulations as described in Section 6 for all existing conditions of the experiment. The experiments are performed below this fuel temperature. At atmospheric conditions the laminar burning velocity of DME–air mixtures is in the same range as that of other hydrocarbons without C=C double bonds [21]. This indicates similar oxidation time scales at high temperatures. At lower temperatures, during the generation of chemical radicals, DME reveals degenerate branching mechanisms [22,23]. This causes a negative temperature coefficient in the temperature-dependent ignition delay times, which is typical for low-temperature oxidation of hydrocarbons [24]. Thus, the properties of DME are suitable for the projected experimental studies.

The high-pressure ignition facility TROJA¹ is built at the *Institut für Kern- und Energietechnik (IKET)* of the *Forschungszentrum Karl-*

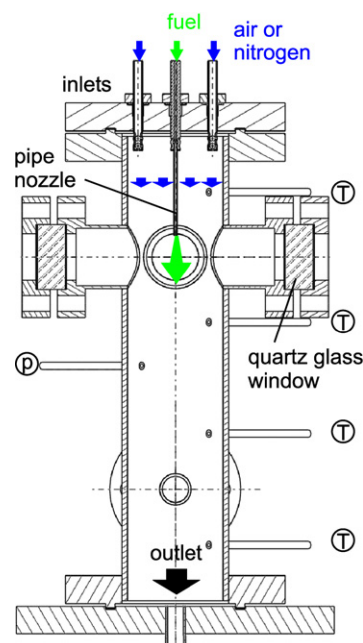


Fig. 1. Cross-section of the high-pressure auto-ignition chamber. Arrows outline the top down flow configuration. Sensor access for pressure (p) and temperature (T) measurements are labeled.

sruhe GmbH, member of the *Karlsruhe Institute of Technology (KIT)*. The ignition chamber consists of a vertically installed cylinder with an inner diameter of 102 mm and an axial inner length of 500 mm (see Fig. 1). The dimensions are large in relation to the jet so that the jet development is not affected by the plenum boundary. The content is continuously purged by heated air during ignition experiments or nitrogen for non-reacting flow measurements. The temperatures and pressures of all gases are controlled and thermal loss prevented by additional wall heatings and thermal insulation. The purge gas is supplied by four short inlets in the top cover. A number of holes in these feed pipes direct the purge gas radially to fill the chamber cross section uniformly and to avoid a preferential flow field in the lower region of the open jet source. The resulting mean axial purge gas velocities are in the range of some cm/s so that background turbulence can be neglected compared with the jet velocity. The injection of pure DME is realized through a single central pipe nozzle. Reservoir pressures of DME up to 7 MPa and DME temperatures around 620 K provide its super-critical state. During the expansion from pressurized DME to chamber pressure atmosphere the gaseous state of the fuel is secured due to the thermodynamic distance in the phase diagram far from the saturated liquid–vapor mixture regime of DME. A high-temperature

¹ Transient Open Jet for Auto-ignition.

high-speed valve releases the super-critical DME into the nozzle. The DME mass flow through the valve is limited to sound velocity because in all working points the fluid-dynamic critical pressure ratio of 1.66 is exceeded. The accuracy of the injection quantity is determined to less than $\pm 1.5\%$ [25] for different pressure ratios. The valve opening starts after a reproducible delay of 0.5 ms due to valve magnetization. The duration of the needle lift is in the sub-millisecond regime. The trigger signal for the valve is synchronized with the data acquisition with an electronic jitter of only $\pm 10 \mu\text{s}$. This ensures exact metering and accurate recording of statistical data. The attached nozzle consists of a 200 mm long pipe that is centrally positioned in the chamber's top cover and that generates a subsonic fuel jet in the chamber. The inner nozzle diameter is $d = 2 \text{ mm}$ so that chamber wall effects become negligible. The jet penetrates a constant high-pressure atmosphere of up to 4 MPa. In the experiments with ignition, the heated air reaches up to 720 K around the nozzle exit. After each cycle of injection and ignition, the nozzle is temporarily scavenged by the post-injection of nitrogen. In this way the nozzle capacity is drained from fuel to prevent the deposition of soot particles out of the flame at the nozzle surface. Residual nitrogen within the nozzle avoids infiltration of oxygen into the nozzle after scavenging. For this reason every new injection cycle induces a preceding nitrogen discharge.

The injection and auto-ignition process can be monitored and analyzed via four windows in the chamber wall which are arranged crosswise (see Fig. 1). A clearance diameter of 50 mm each allows for the application of non-intrusive optical flow measurement techniques (see Fig. 7). A more detailed description of the experimental realization and methods is given in [25]. Different combinations of injection and chamber pressure give variable nozzle exit velocities. The presented results mainly focus on the injections from $p_{\text{inj}} = 7 \text{ MPa}$ to $p_{\text{ch}} = 3 \text{ MPa}$ or 4 MPa.

3. Jet velocity

The evolution and properties of the instationary jet are investigated separately in a nitrogen atmosphere that inhibits chemical reaction. To compare these non-reactive experiments with the reactive case, the time window between fuel inflow and auto-ignition is used, which is obtained from the experiments with reaction in Section 5. The temporal development of the turbulent velocity profile and turbulence data across the nozzle exit are recorded by Laser Doppler Velocimetry (LDV). A standard LDV system by Dantec Dynamics with an argon ion laser and receiving optics for back-scattered light is used. The 2D velocity field in the evolving jet is obtained by Particle Image Velocimetry (PIV). The measurements are performed with a standard PIV system by LaVision. The configuration is conventional with a laser sheet forming unit attached to two pulsed Nd:YAG lasers (532 nm light emission) and a fast double-frame camera that is positioned perpendicular to the laser sheet, similar to the LIF setup in Fig. 7. Both techniques, LDV and PIV, need tracer particles that are seeded into the injection gas. They are generated by atomizing silicone oil with a pressure of 150 MPa directly into the injection pipe system before the aerosol passes the main injection valve. The purge gas is also seeded with silicon oil droplets by immersion through a high-pressure Laskin nozzle assembly before entering the chamber. Since DME is soluble in oil, a depressurization during injection causes droplet degeneration and flow perturbation. Therefore DME is replaced with nitrogen in these experiments. Considering real gas properties, the kinematic viscosity, density and sound velocity of DME at 620 K and nitrogen at 300 K are identical within a tolerance of 10% [25]. This enables the transfer of velocity and turbulence data from cold isothermal nitrogen measurements to DME at conditions of the auto-ignition experiments. The particle size distribution of the tracer provides sufficient flow tracking ability

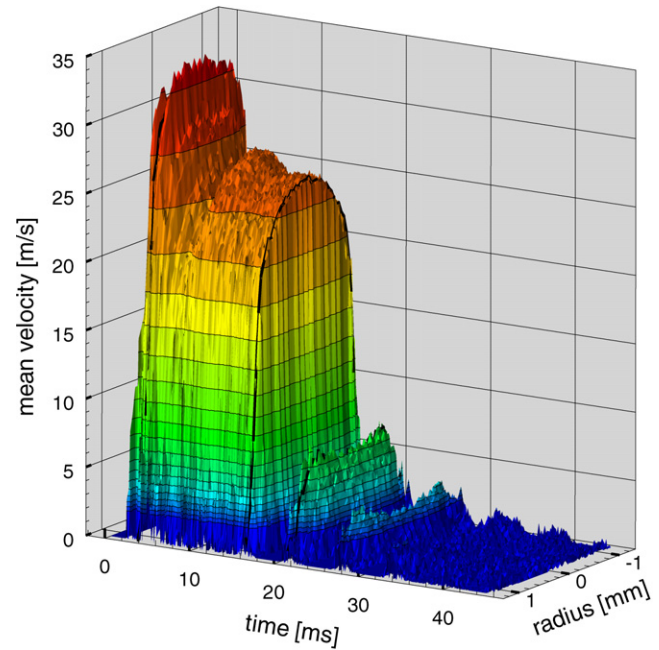


Fig. 2. Temporal evolution of the radial velocity profile at the nozzle exit (injection from 7 MPa into air at 2.5 MPa).

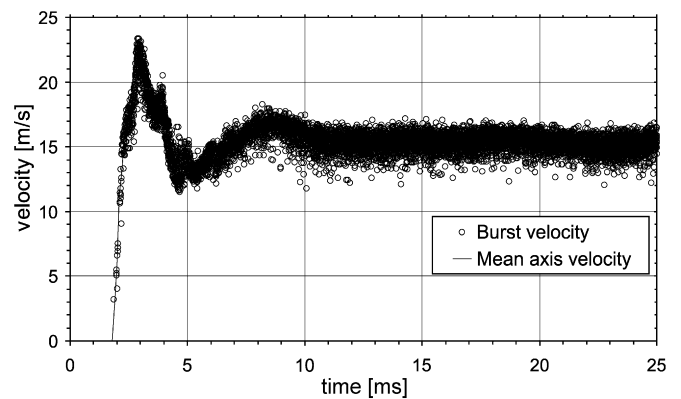


Fig. 3. Burst signals at the jet axis out of 600 injections ($p_{\text{inj}} = 7 \text{ MPa}$, $p_{\text{ch}} = 4 \text{ MPa}$, $t_{\text{inj}} = 50 \text{ ms}$), 0.8 mm downstream the nozzle exit. Shown are the first 25 ms (8500 samples), where different initial oscillation modes occur. After 11 ms the exit flow becomes stationary.

with a mean diameter below $6 \mu\text{m}$ [26]. Errors due to slip between particles and flow are limited to 1% [25].

LDV measurements from different directions show, that the nozzle exit flow is axisymmetric. The LDV probe volume is positioned at $0.4x/d$ below the nozzle and radially traversed with a step size of $50 \mu\text{m}$. The steady-state mean exit velocities at the center can be regulated over the pressure ratio to between 15 and 30 m/s. This corresponds to nozzle diameter based Reynolds numbers between 40,000 and 95,000, respectively, so that the flow is turbulent. The vertical jet is inertia dominated with densimetric Froude numbers in the order of 10^4 [27]. All LDV samples have time stamps relative to the valve trigger signal. The typical temporal evolution of the radial velocity profile at the nozzle exit is shown in Fig. 2 for the injection from 7 MPa into air at 2.5 MPa.

The surface presents ensemble averaged velocities out of 600 injections that are calculated at a time discretization of 0.1 ms. After a dead time of 1.8 ms due to valve magnetization, sound traveling time and flow built-up inside the pipe (see also Fig. 3), the exit flow overshoots with an initially rectangular-shaped mean radial velocity profile.

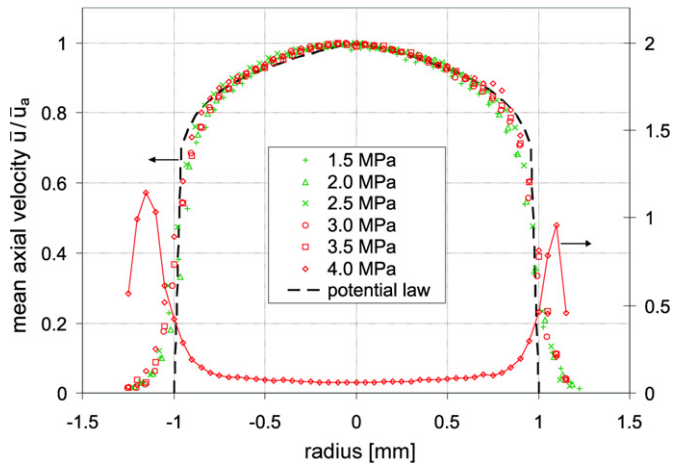


Fig. 4. Steady-state nozzle exit mean velocities for different chamber pressures ($p_{inj} = 7$ MPa), normalized with the maximum velocity at jet axis. The radial core profile is identical to a turbulent potential law with an exponent of $1/9$. The local turbulence level is shown for 4 MPa.

Momentum transfer to the inner wall of the pipe nozzle forces the attenuation to a curved profile after the transition through different modes of oscillation. The dominating longitudinal oscillation has a wavelength of 6 ms or a frequency of 165 Hz. This frequency can be attributed to a first order harmonic from a quarter-wave acoustic resonance in the chamber tube and is also observed after valve closing. The unsteady charging of the injection gas into the nozzle between the high-speed valve and the injection tube generates an excitation spectrum at the beginning of injection. This spectrum emerges a preferred higher frequency mode around 1 kHz coupled to geometric dimensions within the nozzle. Fig. 3 demonstrates the same behavior at 4 MPa air pressure with a longer injection duration of 50 ms. After 11 ms the exit flow velocity becomes stationary. In both, the reactive and LIF experiments, DME reaches the nozzle exit at 16 ms for this pressure ratio, so that the transient fuel injection starts with a constant mean exit speed. By integration of the velocity profile over the nozzle area, the steady-state volume flow rate is 0.040 l/s on a chamber pressure level of $p_{ch} = 4$ MPa ($p_{inj} = 7$ MPa). The steady-state velocity profile is described by a potential law for developed turbulent pipe flows [28]; the core flow fits to an exponent of $1/9$, see Fig. 4. Residual bias results from geometric effects of the LDV probe volume dimension which is not punctiform. Therefore, the measured LDV velocity can differ from the theoretical 3D velocity profile up to -4% in the flow core and up to -8% in the jet boundary layer [25].

In the shear layer the profile broadens due to the acceleration of the surrounding chamber gas. Comparing the mean velocity profiles from all pressure ratios by relating the local mean velocities to the maximum velocity in the axis center, it is shown, that all profiles become congruent. It is found that the mean axis speed is linearly dependent on $[(p_{inj} - p_{ch})/p_{ch}]^{0.5}$ [25]. The measured radial and azimuthal velocity components have zero mean values. The velocity fluctuations (rms) in the axis center are dominant in axial direction and ranges from 5 to 8% of the mean, varying with the pressure ratio. For $p_{inj} = 7$ MPa, $p_{ch} = 4$ MPa the fluctuation in the center is $u_{rms} = 1$ m/s, increasing towards the shear layer with a maximum of $u_{rms} = 3$ m/s; the associated profile of the local turbulence level u_{rms}/\bar{u} is plotted in Fig. 4. The associated histograms exhibit a Gaussian characteristic.

The PIV measurements of the 2D jet velocity field complement the findings from LDV data. The data processing of the captured double frames is performed with DaVis 7 software. The displacement of particle patterns is calculated by cross-correlation algorithms of 50% overlapping interrogation windows. The accuracy is

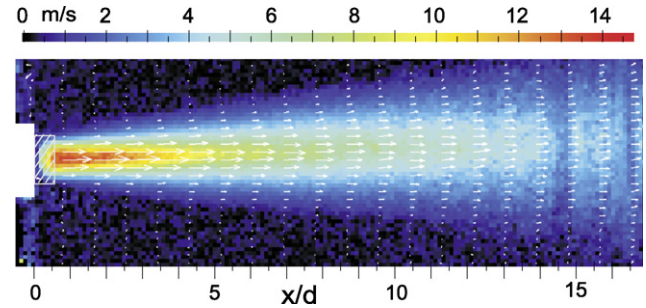


Fig. 5. PIV measurement of the mean stationary jet velocity field of the preceding nitrogen at 20 ms after injection start ($p_{inj} = 7$ MPa, $p_{ch} = 4$ MPa). In the ignition experiments the subsequent DME propagates within this flow field. The gap at $x/d = 14.5$ results from shading due to lens defect. The hatched area is not validated in PIV because of high particle density, but measured with LDV (see Fig. 4).

improved by sub-pixel estimator functions. Adaptive multi pass is applied with decreasing window size to a final window size of 16 pixels. The resulting spatial resolution is 0.44 mm at a grating of 0.22 mm. The thickness of the laser light sheet is 0.55 mm.

During the beginning of the nozzle exit flow—the regime that corresponds to the propagation of the preceding nitrogen jet—a typical head vortex is formed and convected downstream. In all injections, toroidal eddies with different scales are found along the shear layer at same positions for same time steps [25]. This also demonstrates high injection reproducibility. These vortices grow in size but loose magnitude with increasing distance to the nozzle. The data are consistent with LDV information near the nozzle and indicate the temporal and spacial transportation of the found oscillations. At the time when DME enters the preceding nitrogen jet in the reactive or LIF experiments, the eddies are already convected downstream out of the auto-ignition region. All macroscopic characteristics of the nitrogen jet velocity field become stationary before the subsequent fuel leaves the nozzle in the experiments with reaction.

The validation of the computed vectors of the instantaneous vector field is performed by a quality criterion: after subtraction of the background noise in the cross-correlation data the highest detected correlation peak must exceed the second highest peak by a prescribed factor. With a resulting mean factor of 3 the PIV measurements ensure a high correlation quality. Tracer particles are small to limit slip effects with the carrier fluid, but generate peak locking errors in the optical mapping by the camera [29]. With the optimal combination of optical resolution and particle displacement by the pulse width between the laser shots, maximum uncertainties of ± 2.7 m/s in single vectors can occur. With the high number of validated single vectors in the order of 10^3 this error is strongly reduced in the ensemble averaged mean vector field to a 95% confidence interval of ± 0.2 m/s. Only for the statistical data the rms values need correction [25].

Fig. 5 shows the steady state mean velocity distribution at 20 ms after injection, when ignition is probable, see Table 1 for $p_{inj} = 7$ MPa, $p_{ch} = 4$ MPa. The hatched area is not validated because of the high particle density at the nozzle exit, which generates a random speckle pattern in the camera chip. For this area the LDV measurements complement the velocity data consistently (see Fig. 4). The hyperbolic decay of the center line velocity is already revealed at nozzle distances $x/d > 2$. This is represented by the linear dependence of the ratio of the mean nozzle exit velocity to the local mean velocity along the jet axis in Fig. 6.

The fitted straight line in Fig. 6 has a slope of 0.2, which is consistent with other open jet experiments [27]. The virtual jet origin [27] lies at $x_0 = -3d$. The axial spreading rate of the radius at half maximum is $y_{0.5u} = 0.083(x - x_0)$, also with good agreement to other experiments [30]. In the self-similarity regime for

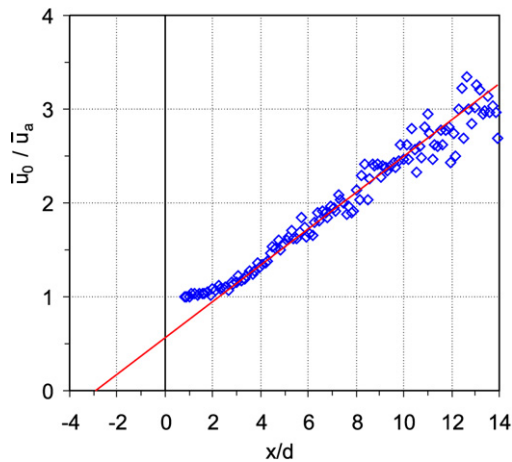


Fig. 6. Ratio of constant mean exit center velocity to local mean axis velocity shows linear dependency on nozzle distance along the jet axis, already from $x/d > 2$ ($p_{inj} = 7$ MPa, $p_{ch} = 4$ MPa). The virtual jet origin is at $x/d = -3$.

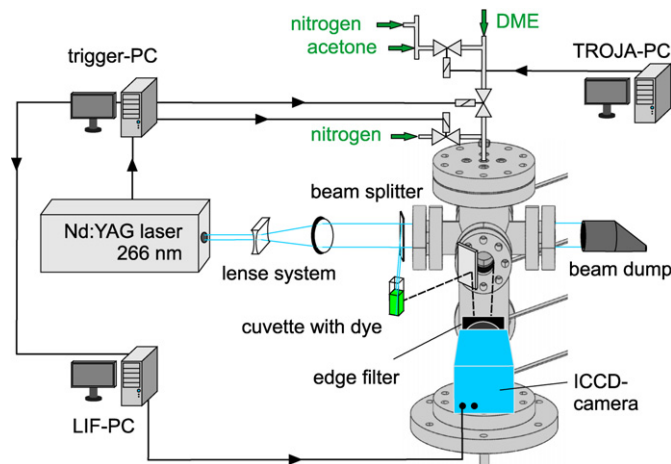


Fig. 7. Experimental setup for the LIF measurement. The pulsed laser beam is formed to a light sheet that is directed through the center of the open jet field inside the chamber. The acetone tracer is added to the DME prior to injection and excited by laser exposure in the jet. The fluorescence light is captured by an intensified CCD camera. A part of the light sheet excites a dye whose fluorescence light is deflected by a mirror to be recorded simultaneously by the camera for correction purpose. Signal lines are presented in black color.

$x/d > 2$ the radial profiles of the mean axial velocities coincide to Gaussian curves when relating the velocities to the maximum axis velocity and the radius to $y_{0.5u}$. The peak locking corrected rms values show that a turbulence level of 30% at the jet axis is already reached at $x/d = 5$. This is consistent with the findings from LDV and LIF experiments.

4. Mixture fraction distribution

The 2D fuel distribution at discrete time steps is studied within the time-frame between DME release into the chamber and ignition. It is measured by planar Laser Induced Fluorescence (LIF) of acetone that is added to DME as tracer gas. The experimental setup is sketched in Fig. 7.

From a pulsed Spectra-Physics Nd:YAG laser, the fourth harmonic wavelength 266 nm is generated to excite the acetone tracer. A lens system is aligned with the ignition chamber and forms a laser light sheet with a thickness of 0.2 mm beneath the pipe nozzle. The preheated acetone tracer is injected directly into the DME by an additional high-speed injector. From the TROJA-PC (Fig. 7) the small tracer quantities are controlled exactly. Evapora-

tion and mixing is accomplished prior to release into the pipe nozzle. The concentration of acetone in DME is constant and limited to less than 10 vol%. The high miscibility between the two gaseous media ensures the uniform dispersion of both during the turbulent jet propagation outside the nozzle. Chemical reaction in the chamber is avoided by injection of the acetone-loaded DME into a nitrogen atmosphere that is pressurized and temperature-controlled as in the experiments with reaction. Because fuel consumption during radical generation before auto-ignition is marginal in the case with air in the chamber, the measurement in the nitrogen atmosphere is justified. When the stimulation energy by the laser keeps beneath the saturation for fluorescence, the expected signal S_f follows [31,32]:

$$S_f(\lambda, T) \propto \frac{x_{\text{acetone}} p}{RT} I_{\text{laser}} \sigma(\lambda, T) \Phi(\lambda, T), \quad (1)$$

with the mole fraction x_{acetone} , pressure p , universal gas constant R , laser energy I_{laser} , absorption coefficient σ and fluorescence yield Φ . Because the absorption coefficient of acetone is comparatively weak, a pressure dependency is neglected [31,32]. In the interesting pressure range, the fluorescence yield of acetone remains constant with nitrogen as collision partner [33]. At the excitation laser wavelength of 266 nm the absorption coefficient σ possesses very small sensitivity to temperature fluctuations within the existing temperature range [31]. DME transmits light between 200 and 450 nm [34] and does not react with acetone, so that the representative measurement of acetone is not affected. Data on the temperature dependence of the fluorescence yield at high pressures do not exist. But testing on an open jet with a temperature difference of 100 K between injection and chamber gas shows no difference to the measured data of an isothermal jet field. Hence, the temperature dependence is assumed to be negligible in the measurement under interesting conditions. The linear dependency between tracer mole fraction x_{acetone} and fluorescence intensity S_f is checked affirmatively.

Outside the chamber, a fraction of the laser light sheet is also directed to a quartz cuvette (see Fig. 7). It contains a dye solution for correction of the non-uniform spatial laser intensity. An intensified CCD camera with UV-Nikkor objective collects the fluorescent light simultaneously from both the open jet and the cuvette. An edge filter in front of the objective suppresses laser light reflections. The data is obtained as instantaneous 2D images that are quantified after a multi-step correction procedure [35]. This comprises remaining laser background reflection, camera pixel sensitivity, integral power of single laser shot, variable light intensity along laser sheet and long-term varying tracer seeding rate. The results are reported in terms of the molar mixture fraction X that is derived from the measured mole fraction x_{acetone} [36]:

$$X = \frac{x_{\text{acetone}} - x_{\text{acetone},\infty}}{1 - x_{\text{acetone},\infty}}. \quad (2)$$

After every series for a single time step, the mean fluorescence signal at the nozzle exit of the steady-state jet is measured for reference (“1” in Eq. (2)). Each time step of 1 ms involves an image number of 100 single injections that enables conditional ensemble statistics.

In Fig. 8 the measured 2D molar mixture fraction X is shown at 15 ms after start of injection from $p_{inj} = 7$ MPa to $p_{ch} = 3$ MPa, when ignition is probable under oxidative conditions (compare with Table 1).

This pressure ratio is presented because of the higher exit velocities that lead to longer axial fuel penetration than with $p_{ch} = 4$ MPa. For technical reasons the temperature for the injection gas (DME with acetone) is limited to $T_{inj} = 500$ K. The nitrogen in the chamber near the nozzle exit has a temperature of $T_{ch} = 680$ K.

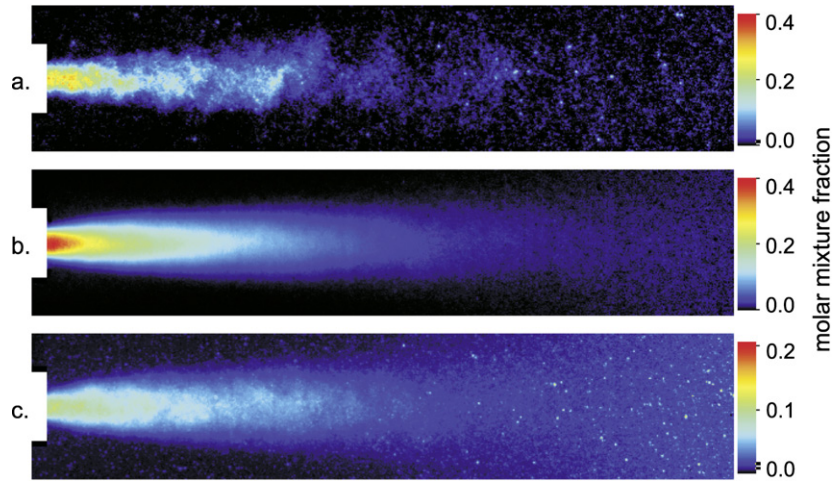


Fig. 8. 2D distribution of the molar mixture fraction X of DME at the ignition-probable overall time step of 15 ms ($p_{\text{inj}} = 7$ MPa, $p_{\text{ch}} = 3$ MPa): (a) single injection, (b) mean out of 100 injections with corresponding rms values (c).

Table 1

Ignition delay times for different pressure ratios ($p_{\text{inj}} = 7$ MPa, $T_{\text{inj}} = 620$ K, $T_{\text{ch}} = 720$ K)

Chamber pressure, p_{K}	DME inflow at	Effective ignition delay time (95% confidence interval)
2 MPa	8 ms	3.0 ± 0.72 ms
3 MPa	11 ms	3.4 ± 0.73 ms
4 MPa	16 ms	3.3 ± 0.72 ms

The instantaneous DME distribution in Fig. 8a shows high macroscopic fluctuations during the discharge into the preceding nitrogen jet (see Section 3). The photon shot noise by free electrons in the detector chip remains as brighter pixels because digital filtering is omitted, but does not influence the statistics of the large data volume. The mean 2D molar mixture fraction field out of 100 injections is conditionally built for the same time step and charted in Fig. 8b. The corresponding rms values in Fig. 8c show relative mixture fraction fluctuations between the different injections of up to 30% at the nozzle exit. The mixture fraction field at this ignition-probable time step is also shown in the mean sequence of Fig. 9.

Prior to DME release, a weak accumulation of acetone is visible within the boundary of the preceding stationary nitrogen jet because the tracer is not completely drained due to geometric constraints within the nozzle. In front of this background signal the DME fraction significantly raises. The evolution of the radial molar mixture fraction in Fig. 10 confirms this behavior and shows Gaussian temporal (Fig. 10a) and spatial (Fig. 10b) distribution.

Deviations are due to laser light extinction after Beer–Lambert’s law. At earlier time steps during instationary evolution the mixture fractions are small, so that radial profiles are symmetric within 2%. By considering only the laser facing half of the jet (negative radius) the remaining maximum errors occur at the jet axis near the nozzle, which are limited to 5% for the latest ignition probable time step. Downstream, along the jet axis, the mean mixture fraction decays hyperbolically for every time step i according to $(X - a_i) = b_i(x - c_i)^{-1}$. The hyperbolas are shown as smooth lines in Fig. 11. From the parameters a_i , b_i and c_i no conclusive time law can be derived.

For comparison, the transient and stationary mean axis profiles are plotted for both $p_{\text{ch}} = 3$ MPa and 4 MPa. The axial spreading rate of the radius at half maximum in mixture fraction is constant for all pressure ratios. Its value is $0.12x/d_e$ with the equivalent nozzle diameter $d_e = d[\rho_0/\rho_\infty]^{0.5}$ being $1.5d$ in these experiments. The very short transition length to self-similarity, both in the mixture fraction and in the velocity field, is a new finding. In a sta-

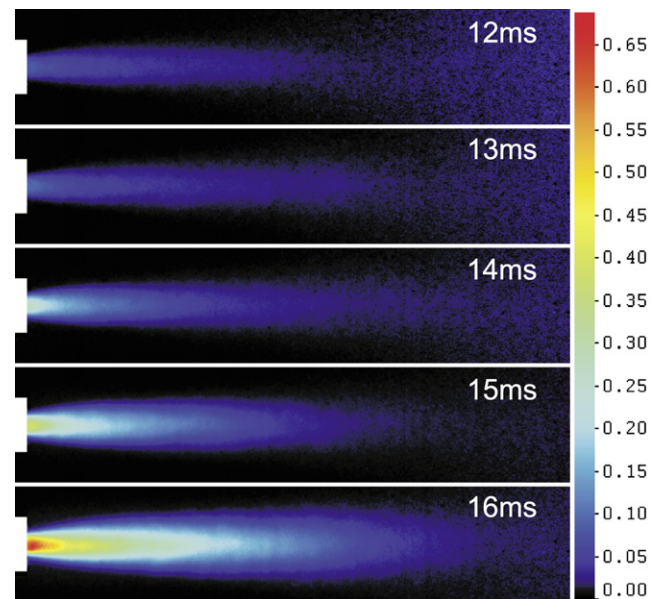


Fig. 9. Phase-averaged evolution of the inert molar mixture fraction X within the time-frame between DME inflow and auto-ignition ($p_{\text{inj}} = 7$ MPa, $T_{\text{inj}} = 480$ K, $p_{\text{ch}} = 3$ MPa, $T_{\text{ch}} = 690$ K).

tionary open jet the self-similarity region starts for $x/d > 10$ when enough air is entrained into the fuel jet [37]. Here, the unsteady charging of the injection tube via the high-speed valve causes nitrogen entrainment within the nozzle. Similar observations are reported by [38].

The local distribution of X is derived from a 3×3 pixel area to increase the data volume to 900 values and to match with the PIV grating and the laser sheet thickness. The resulting spatial resolution is $200 \mu\text{m}$. The histograms are each normalized with the total number of values to obtain discrete PDFs. Thus, the probability of occurrence of the mixture fraction X is measured, which is subdivided into bins of width 0.01. It is found that all PDFs are unimodal within the complete jet area for all time steps. In the Figs. 12 and 13, the PDFs of selected points at the most likely ignition time step are shown along the jet axis and along the radius, respectively.

In each case the distributions narrow towards the jet boundary with a decreasing mean mixture fraction. The lines represent Beta functions of the form [39]:

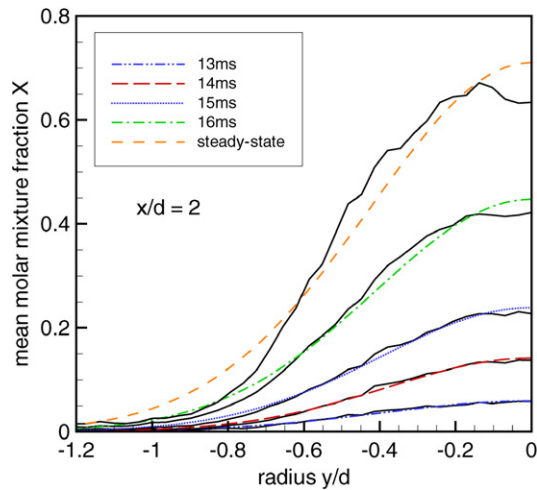
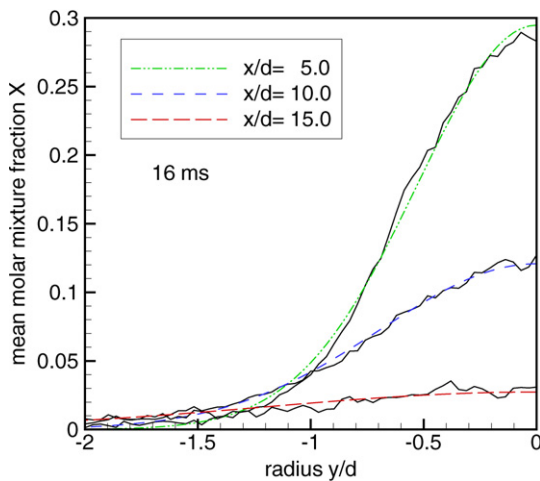
(a) Temporal evolution at $x/d = 2$.(b) Spatial evolution for $t = 16$ ms.

Fig. 10. Radial distribution of the mean molar mixture fraction X for conditions in Fig. 9. The curves can be considered to be Gaussian (smooth lines); deviations from it at higher mixture fractions (steady-state jet after 24 ms) results from increasing laser absorption.

$$\text{PDF}(X) = \gamma X^{\alpha-1} (1-X)^{\beta-1}, \quad (3)$$

$$\gamma = \frac{\Gamma(\alpha + \beta)}{\Gamma(\alpha)\Gamma(\beta)}, \quad (4)$$

where γ is the Gamma function. This formulation contains the parameters α and β that are calculated from the local mean \bar{X} and the variance \bar{X}'^2 in the following way:

$$\alpha = \left(\frac{\bar{X}(1-\bar{X})}{\bar{X}'^2} - 1 \right) \bar{X}, \quad (5)$$

$$\beta = \alpha \left(\frac{1}{\bar{X}} - 1 \right). \quad (6)$$

The agreement between the distributions in Figs. 12 and 13 and the independently calculated curves of the Beta functions is significant. Maximum mean squared errors (MSE) between measured histograms and associated Beta functions are in the order of 10^{-3} at the jet edge and in the order of 10^{-5} within the jet core region. Outside the jet, the mixture fraction X is zero; noise leads to artificial values for α and β , as shown in Fig. 14, where all calculated parameters within the laser sheet are plotted.

The description of mixture fraction with Beta functions within the overall jet region simplifies PDF modeling considerably—especially in the context of presumed PDFs. This finding is new for

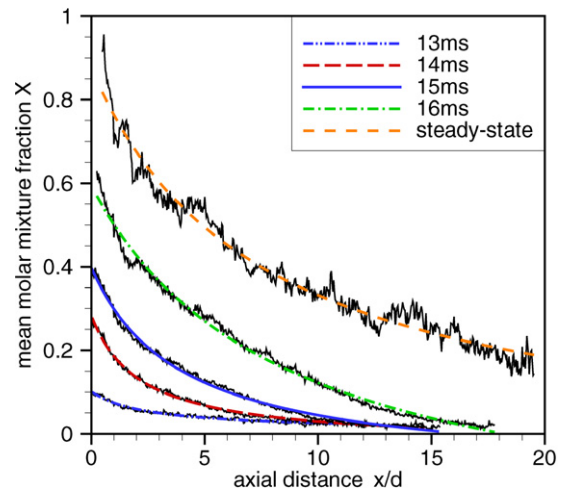
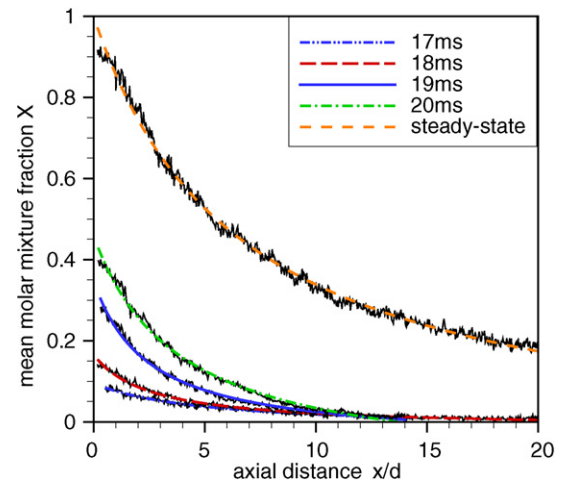
(a) $p_{\text{ch}} = 3$ MPa.(b) $p_{\text{ch}} = 4$ MPa.

Fig. 11. Temporal evolution of the mean molar mixture fraction along the axis ($y/d = 0$) at different pressures. Each decay along x/d can be described as hyperbolic (smooth lines). For conditions see Fig. 9.

the present configuration of the instationary open jet. The transient evolution of the discrete PDF of DME mixture fraction X is shown in Fig. 15 for a representative location within the shear layer of the jet.

For later time steps, both the mean and the fluctuations in X increase with the same characteristics as described for the spatial evolution.

By integrating the measured PDFs between the atmospheric flammability limits of DME (3–18.6 vol% in air [19]), an indication of idealized local ignition probability is deduced—omitting for the moment the influence of temperature and flow distribution. The results are shown as 2D fields during the transient and stationary DME discharge in Fig. 16.

With this definition the weak acetone contamination in the preceding nitrogen leads to higher values of the ignition probability near the nozzle exit. Substantially, Fig. 16 confirms the flammability of the transient fuel jet. During the experiments with reaction, the nitrogen jet intakes hot air into the subsequent release of DME, so that molecular mixing and radical generation starts with DME entering the chamber. This is further addressed in Section 6.

5. Auto-ignition

The determination of the temperatures of DME and air is essential because chemical kinetics depends exponentially on tem-

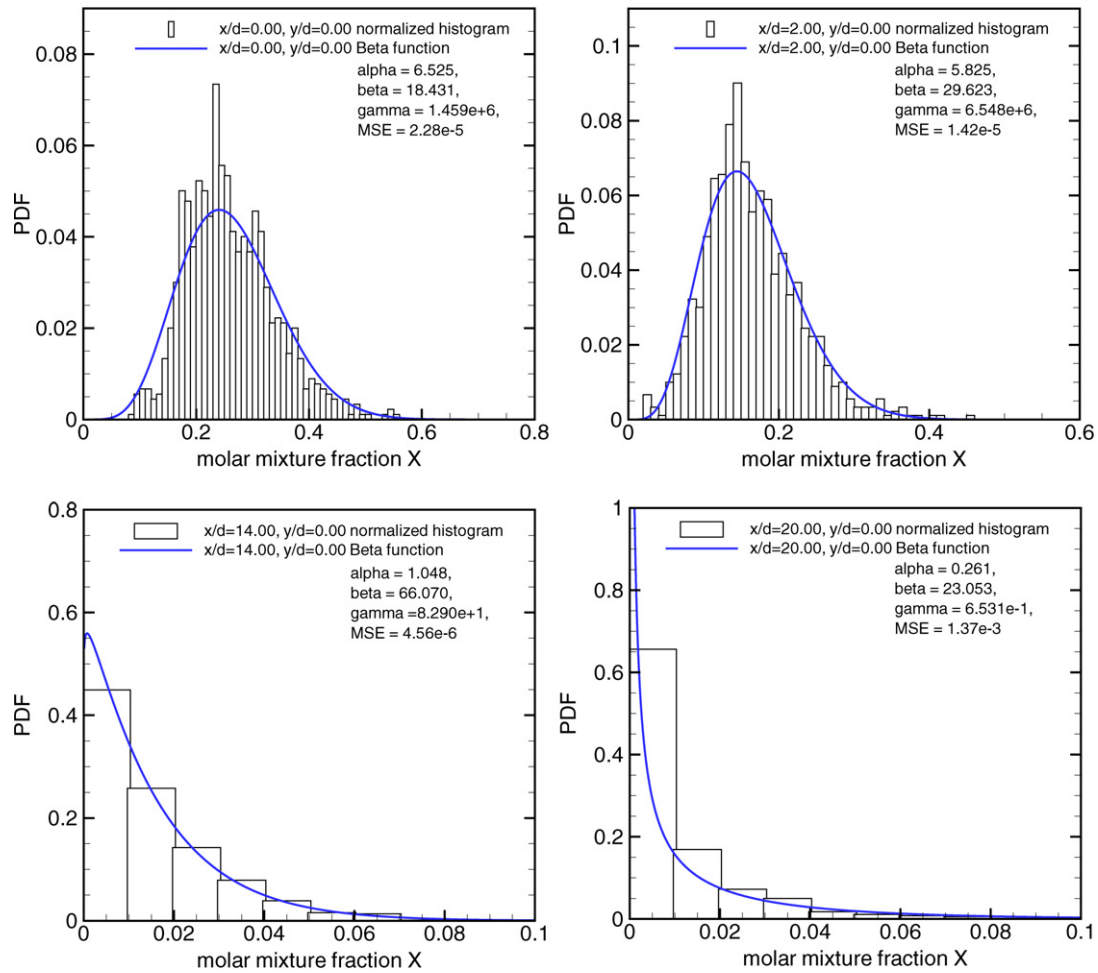


Fig. 12. Selected histograms along the jet axis ($y/d = 0$) from $x/d = 0$ to 20 ($p_{inj} = 7$ MPa, $p_{ch} = 4$ MPa) at the most likely ignition time of 19 ms. The distribution complies with Beta functions calculated independently from the mean and the variance of X .

perature. The temperature of the injection gas is measured with thermocouples inside the high-speed valve. At DME temperatures, which are realizable with the TROJA facility, the isenthalpic expansion into the pipe nozzle causes a temperature decrease of only 10 K. The residence time of the DME within the nozzle is three orders of magnitude shorter than the relaxation time for heat transfer from the hotter pipe nozzle to the gas. Further heating of the gas flow is therefore insignificant. The typical expected injection gas temperature at the nozzle exit is 620 K, which is coupled to the maximum air temperature at the upper inlet of the chamber. Due to thermal stratification within the chamber, the chamber gas at the height of the nozzle exit is lower compared to the chamber inlet condition. The chamber gas temperature is measured by thermocouples that are located inside the chamber but outside the jet (Fig. 1). Additional experiments with a traversed thermocouple around the nozzle exit, corrected for heat conduction and radiation, validated the thermocouple measurement of the chamber gas from the two upper measurement levels. They indicate an air temperature of 720 K around the nozzle exit at maximum steady-state chamber conditions. The experiments with reaction are performed under these conditions.

The auto-ignition during the instationary jet propagation increases the chamber pressure less than 1% of the pressure level because the reacting volume is small compared to the chamber volume. Therefore the auto-ignition is recorded by high-speed shadowgraphy. Because the refractive index of DME is different from that of the surrounding air, concentration gradients of the DME jet prior to ignition are visualized. Not only the Schlieren from DME

inlet is detected: during auto-ignition the temperature of the fuel-air mixture rises and involves gas expansion. Because temperature gradients also have an effect on the optical density, the chemical reaction is detected concurrently. Thus, the moment of hot gas expansion is identified, see Fig. 17 and Movie 1.

The overall ignition delay time is quantified as ignition time related to the trigger signal of the high-speed valve. With a video frame rate of 1 kHz the signal is integrated over 1 ms exposure time in each frame. The observed moment of ignition is set at the center of the frame exposure time. Then the symmetric detection error becomes ± 0.5 ms. This procedure is equally performed for the moment of fuel inflow within the same video sequence, see mean values in Table 1. The time of detected fuel discharge is then subtracted from the overall ignition time to obtain the effective ignition delay time. The progress of injection and auto-ignition is repeated only once in a minute to allow for scavenging the exhaust gas.

The behavior of the auto-ignition shown in Fig. 17 is identical for all studied conditions of pressure ratios and temperatures. No hot spot ignition is captured. The heat generation from chemical reaction is almost synchronous over a wide spatial extension. It can be concluded that the ignitable part of the open jet reacts simultaneously within this area. The Schlieren development due to chemical heat is too fast to be explained by turbulent flame propagation. This is verified by videos at a 10 kHz frame rate (Movie 2).

For a high number of repetitions, Fig. 18 displays the ignition delay times that are statistically unimodally distributed around

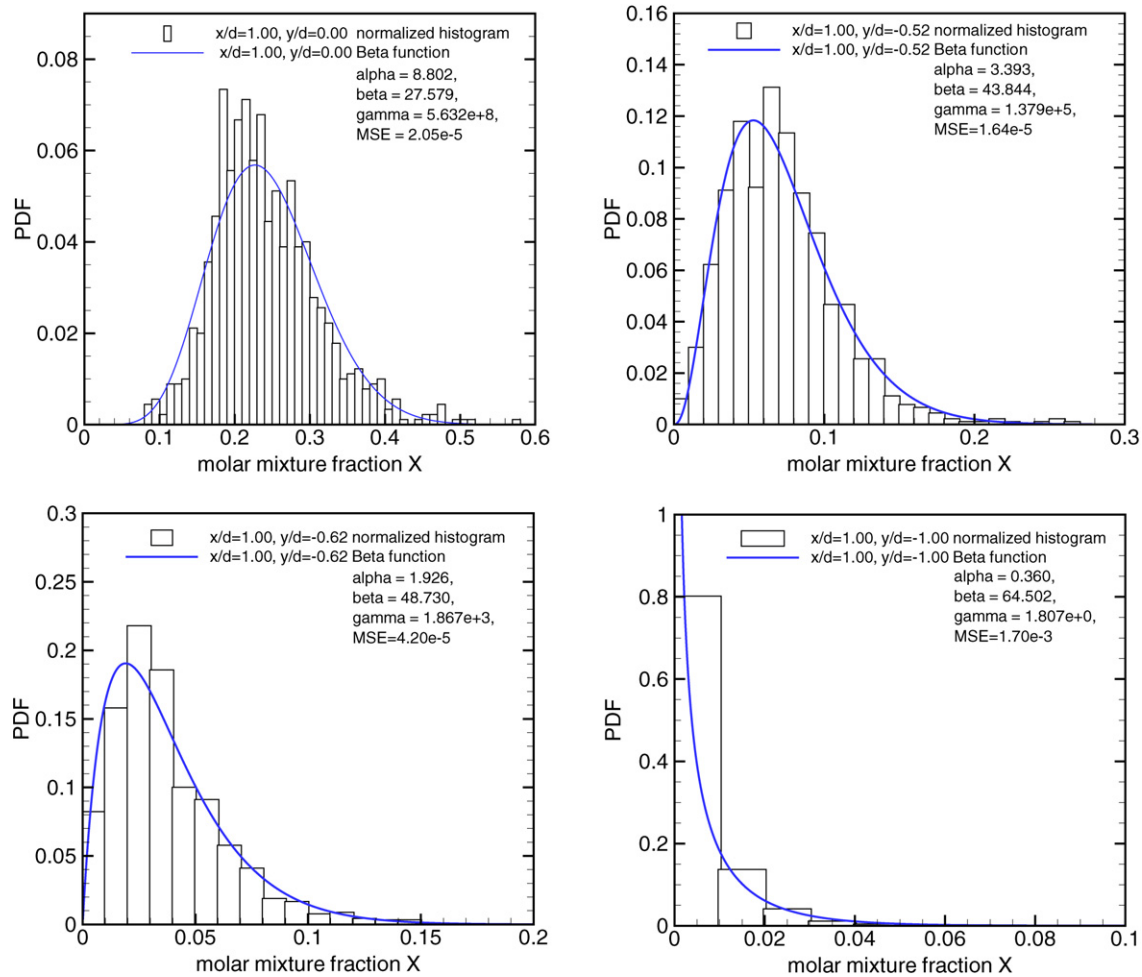


Fig. 13. Selected histograms along the radius at $x/d = 1$ from $y/d = 0$ to 1 ($p_{inj} = 7$ MPa, $p_{ch} = 4$ MPa) at the most likely ignition time of 19 ms.

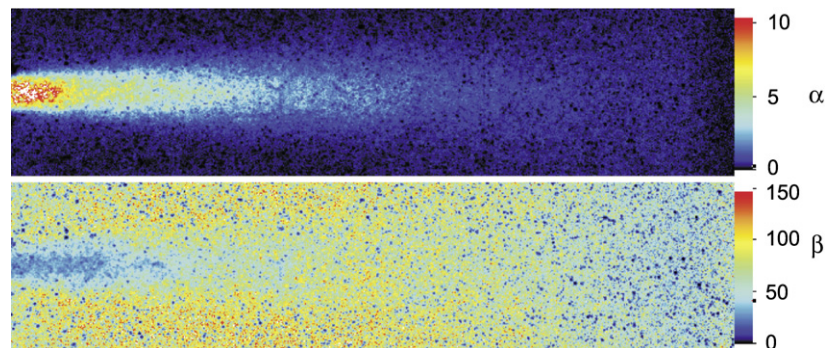


Fig. 14. 2D distribution of the Beta function parameters α and β , compare with Figs. 12 and 13.

a mean of 3.3 ms. Different injection and chamber pressures are applied to vary velocity and turbulence of the DME jet (Table 1).

But Fig. 19 shows that the effective ignition delay times are marginally affected. With higher mean jet speeds the region of ignition is only shifted downstream. The implied variation of mixing time scales do not influence the slower chemical kinetics. Because the slower process governs the auto-ignition dynamics, chemical kinetics is predominant over the mixing process between air and fuel. This behavior supports the theory of independent flamelets that experience a history of mixing and reaction while traveling downstream with the jet. Flamelet calculations in Section 6 confirm consistency.

At a higher sampling rate of 10 kHz even the two-stage temperature progression within the auto-ignition process is resolved. The visible section is then reduced to an area of 6.7×18 mm, see Movie 2. On the video sequence the turbulent flow field of the DME-air mixture is seen firstly. After a first induction period the entire flow field expands instantly due to a first temperature rise. Then the intensity of structural contrast remains constant during a second time period. Subsequently, a much stronger increase in flow structure and gas expansion follows due to the higher heat release of the second ignition stage. Afterwards the reaction zone of a non-premixed flame evolves. This characteristic is typical for hydrocarbons in the low temperature oxidation regime: The major temperature rise follows a period of degenerating chain branching

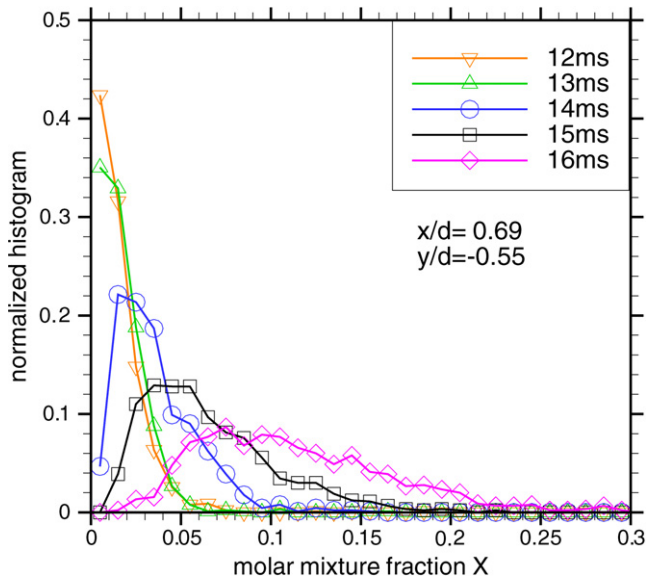


Fig. 15. Instationary evolution of the discrete PDF of DME mixture fraction X in the jet shear layer at nozzle distance $0.69d$ and radius $0.55d$ (injection from 7 MPa, 480 K into nitrogen at 3 MPa, 690 K). The distributions comply with Beta functions and broaden during transition to the most likely ignition time of 16 ms.

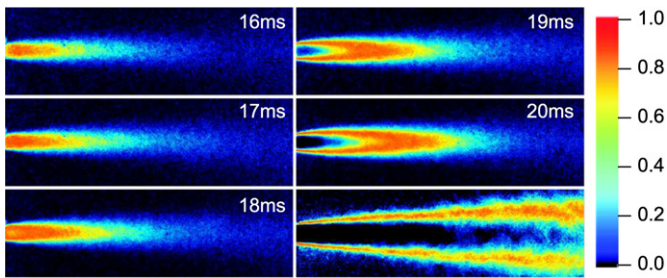


Fig. 16. Local ignition probability, see text (DME injection from 7 MPa, 480 K into nitrogen at 4 MPa, 690 K). From reactive experiments, the most likely overall auto-ignition time in air is 19 ms. For comparison, the steady-state mixture fraction field is shown at bottom right.

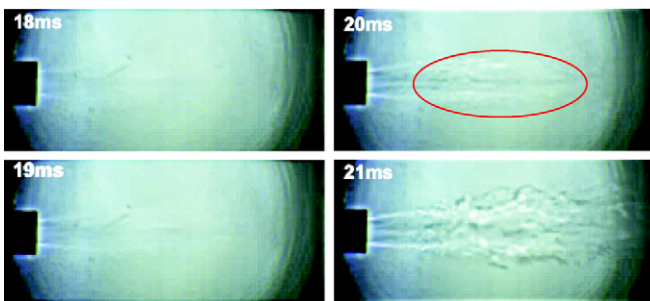


Fig. 17. Shadowgraph of injection and auto-ignition sequence (marked ellipse) in a DME fuel jet (injection from 7 MPa, 600 K into air at 4 MPa, 720 K, DME emerges at 17 ms, ignition occurs at 19.5 ± 0.5 ms). The visible outer diameter of the nozzle is 4 mm. For improvement of contrast, unsharp masking is applied as image post-processing. The complete sequence is shown in Movie 1.

that occurs after a lower first reaction phase. This phenomenon is addressed in more detail in the flamelet study of the next section. With the reduced visible image section, the start of DME flow out of the nozzle and the moment of the initiating distributed reaction zone cannot be captured in the same shadowgraph image. Therefore the overall times of the detected first and second ignition stage are displayed in the scatterplot of Fig. 20. Both time scales are relative to the valve trigger, i.e. without subtraction of inflow time.

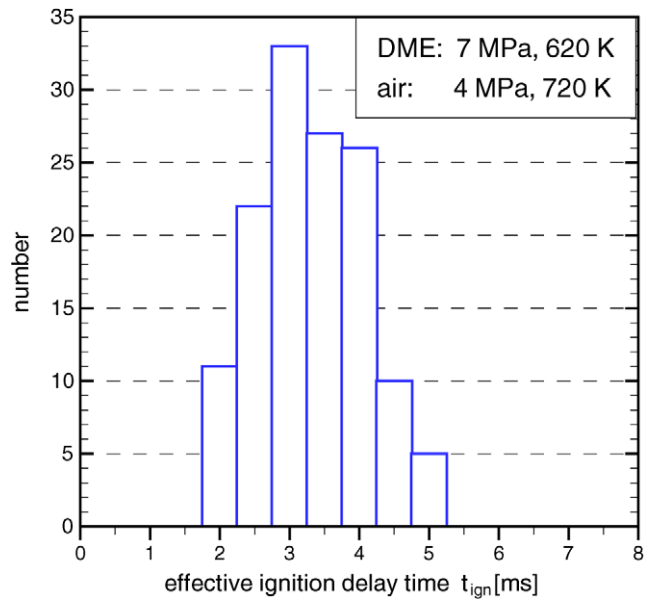


Fig. 18. Histogram of effective ignition delay times ($p_{inj} = 7$ MPa, $T_{inj} = 620$ K, $p_{ch} = 4$ MPa, $T_{ch} = 720$ K).

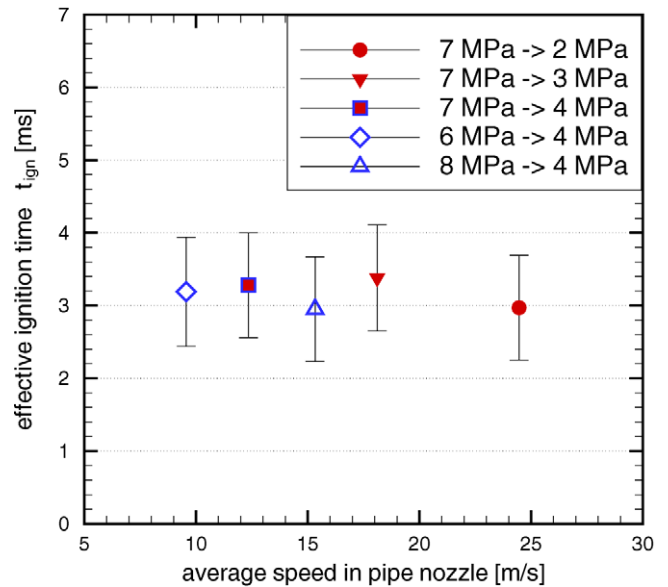


Fig. 19. Mean ignition delay times with 95% confidence interval (bars) for different pressure ratios; compare with Table 1.

Each point represents one auto-ignition with the first ignition delay time at the abscissa and the second at the ordinate; the two outlier points result from reduced injection pressure so that inflow is delayed. The measured time difference of the two ignition stages is $\Delta\tau = 1.4$ ms.

6. Flamelet study

The ignition behavior of the studied transient jet points at kinetically controlled auto-ignition. Therefore time-resolved flamelet simulations by the program INSFLA [7] are performed to complement the experimental findings. This code calculates instationary ignition processes in laminar systems. Transport equations are solved for one-dimensional geometries. Chemical source terms are determined by a detailed reaction mechanism for DME [1,2]. In flow configurations, the approximation for boundary layer flows is applied. The flamelet is calculated with detailed transport with-

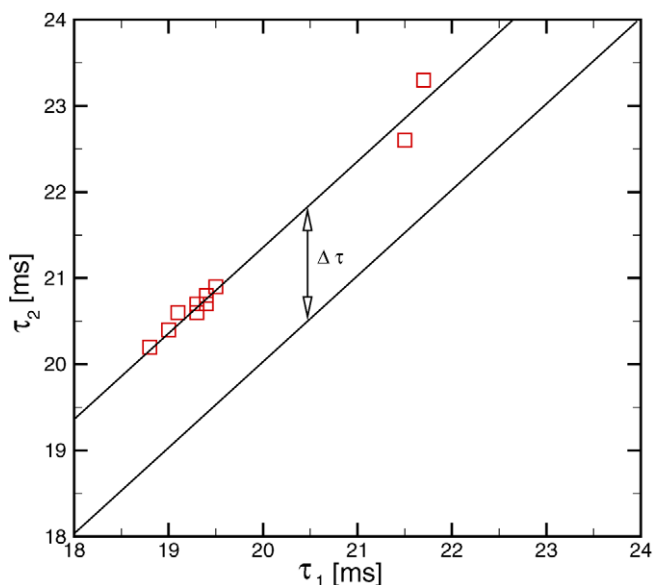


Fig. 20. Correlation between the first and second ignition delay time, relative to the valve trigger signal ($T_{inj} = 620$ K, $T_{ch} = 720$ K).

out explicit study of the influence by differential diffusion. Further details on the implemented algorithms can be found in [7]. The impact of turbulence is assessed by a strain rate parameter [40] that is implemented as described by [41]. The thermodynamic system is isobaric according to the constant pressure atmosphere in the experiments. The time- and space-dependent results are expressed in terms of species concentrations, velocity, temperature and density.

In a first step, calculations are done without initial strain to study the dependency of ignition delay times on chamber pressure and temperatures of air and DME. The 1D calculation domain for high pressures has a length of 2 mm to ensure that no temperature or species gradients reach the grid edge even some time after ignition. The initial flamelet orientation is considered to be spanned across the jet boundary, radially from the jet axis to the pure air field outside the jet. Because the fuel jet is flammable at the nozzle exit (Fig. 16), a single flamelet is notionally exposed at the nozzle exit analog to [42]. The concept of evolving flamelets has been used extensively in the context of representative interactive flamelets (RIF concept). During the convective downstream flow, DME and air are mixing lamarily inside the flamelet. At this internal boundary layer the mole fraction profile of DME and the temperature profile are defined as one-sided Gauss functions [8] as shown in Fig. 21.

For the chosen number of nodes the grid resolution within the border line is 8 μm . Grid independence of the solutions is ensured. In Fig. 22 the typical evolution of the maximum temperature in the domain and maximum mole fractions for selected species is shown for 4 MPa.

Starting at the initial maximum temperature of air (720 K) the peroxy radical $\text{CH}_3\text{OCH}_2\text{OO}\cdot$ is formed due to low-temperature oxidation. In Fig. 22 the first ignition delay time $\tau_1 = 2.97$ ms is defined at the turning point of the maximum temperature progression. The first ignition stage is localized at a lean DME mole fraction of 0.044 which can be considered as ‘most reactive’ like in [8]. For comparison the stoichiometric mole fraction of DME in air is 0.065. The highest reactivity on the lean side corresponds to the higher temperature sensitivity of chemical kinetics compared to the weaker dependency on fuel concentration. The temperature rise leads to degenerate branching in the region of negative temperature coefficient (NTC) of chemical kinetics, so that further building of peroxy radicals is retarded. Due to the high pres-

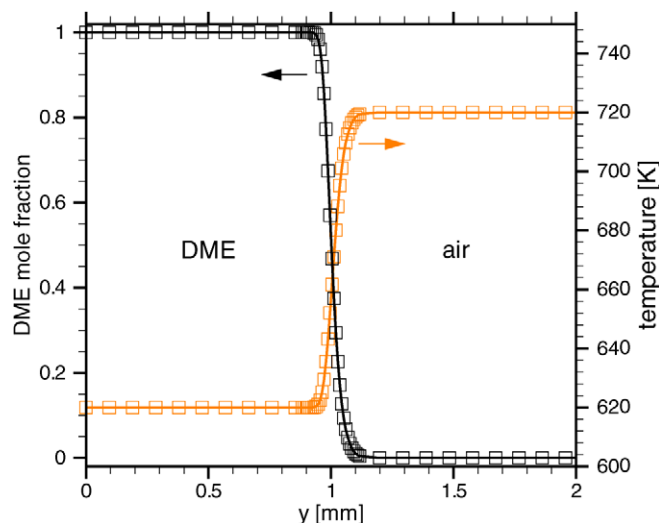


Fig. 21. Initial profile of DME mole fraction and temperature distribution along the 1D computational grid. At the borderline between DME (620 K) and air (720 K) the initial node distribution is condensed to a resolution of 8 μm .

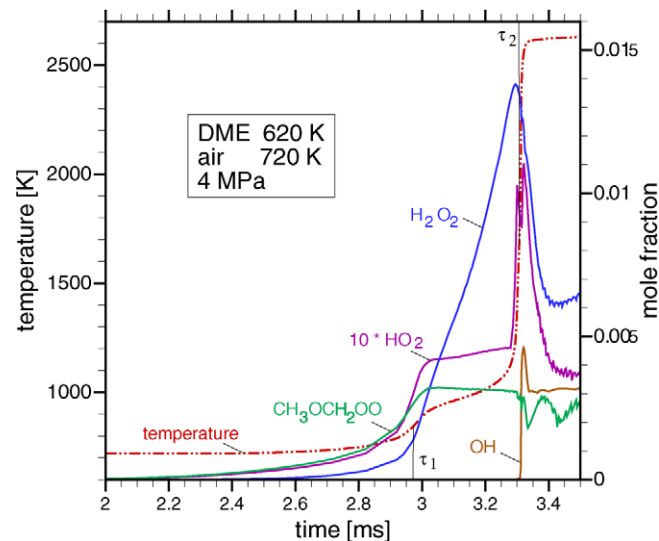


Fig. 22. Temporal evolution of maximum flamelet values for temperature and mole fraction of selected species ($p = 4$ MPa, $T_{\text{DME}} = 620$ K, $T_{\text{air}} = 720$ K). The two-stage ignition is seen in temperature progression; the chemical behavior of the low-temperature oxidation is described in the text.

sure, the recombination reaction $\text{H}\cdot + \text{O}_2 + \text{M} \rightarrow \text{HO}_2\cdot + \text{M}$ takes place [4]. The hydroperoxy-radical $\text{HO}_2\cdot$ reacts with fuel (RH) to hydrogen peroxide (H_2O_2) according to $\text{HO}_2\cdot + \text{RH} \rightarrow \text{H}_2\text{O}_2 + \text{R}\cdot$. This is seen after τ_1 in Fig. 22, when H_2O_2 mole fraction increases. With the associated heat release, the temperature increases until the second ignition stage takes place at $\tau_2 = 3.31$ ms. Then the major temperature rise in the flamelet occurs together with the decomposition of H_2O_2 into hydroxyl radicals ($\text{OH}\cdot$). The high-temperature oxidation then predominates the radical generation in the subsequent non-premixed flame. The flame reaches a maximum temperature of 2630 K. Compared to the histogram of effective ignition delay times in Fig. 19, the first and second ignition delay times from the calculation are in very good agreement with the experimental results. Only the computed second ignition delay time occurs systematically earlier compared to the experimental time difference $\Delta\tau$ in Fig. 20. This is due to multi-dimensional turbulence effects of the real jet that provoke heat loss to the more temperature-sensitive chemistry of the second stage [43], which results in higher $\Delta\tau$.

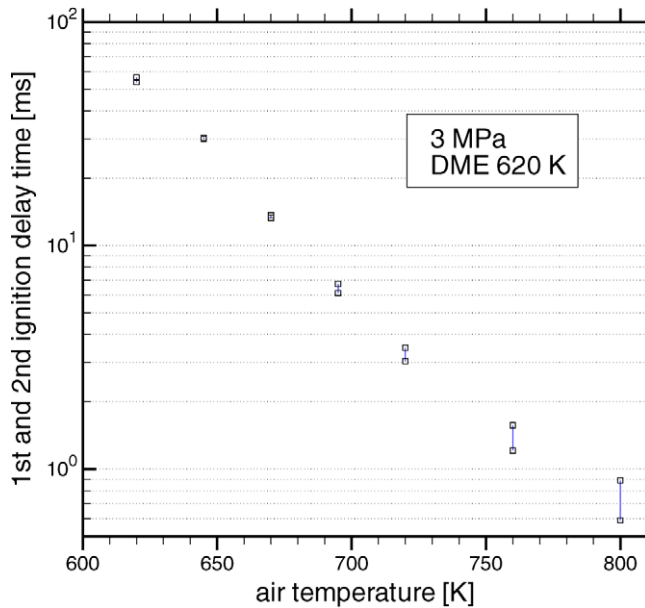


Fig. 23. The influence of air temperature on auto-ignition ($p = 3$ MPa, $T_{\text{DME}} = 620$ K). Paired points indicate first and second ignition delay time.

Further calculations are performed to analyze the influence of temperature and pressure of air and DME on the ignition delay times. Maintaining the initial temperatures and varying the pressure show barely any effect on ignition delay times within the pressure regime from 1 to 4 MPa. Similarly, the ignition delay times are affected only marginally with the variation of the DME temperature at constant pressure and air temperature. The main influence on ignition delay time results from exclusive variation of air temperature which is demonstrated in Fig. 23 for 3 MPa. This effect is in agreement with [9].

An increase or decrease of 80 K in air temperature produces tenfold lower or higher ignition delay times, respectively. For a variation of ± 10 K in air temperature near the nozzle the calculations show a variation between 2.5 and 4 ms in ignition delay time. Thus, the width of the ignition delay time distribution in Fig. 18 (4 MPa) can be explained by temperature fluctuations of the entrained air.

The influence of turbulence on auto-ignition is also studied numerically. The impact of convective flow on a fluid element can be described in a general formulation for stretch [40]. For the simplified configuration in Fig. 21, the stretch is imposed on the borderline of DME and air by countercurrent flow of DME from the left-hand side (positive velocity) and air from the right-hand side (negative velocity) along the computational grid direction y . The inflow velocities at the grid boundaries are kept constant. The resulting velocity distribution of the non-reacting flow field is stationary and linear over y ($dv_y/dy = \text{const}$). With the specified velocities at the boundaries and therefore inflow momentum, it is ensured that the zero velocity in the stagnation plane ($v_y = 0$) coincides with the location of the mixing layer in the middle of the grid in Fig. 21. The effective stretch is the strain perpendicular to the flow direction y . Because the cross flow is modeled as potential flow, the strain rate parameter is $a = 0.5dv_y/dx$ [44]. The potential auto-ignition within the mixing layer is then affected by strain that lead to convective heat loss and transportation of radicals out of the mixing zone. In the jet shear layer the turbulence acts on this flamelet, which is convected downstream. The physical and chemical history of the flamelet in time is studied with calculations for different strain rates a .

Fig. 24 shows the continuous grow from both, first and second ignition delay times, with increasing strain rate for 3 MPa and

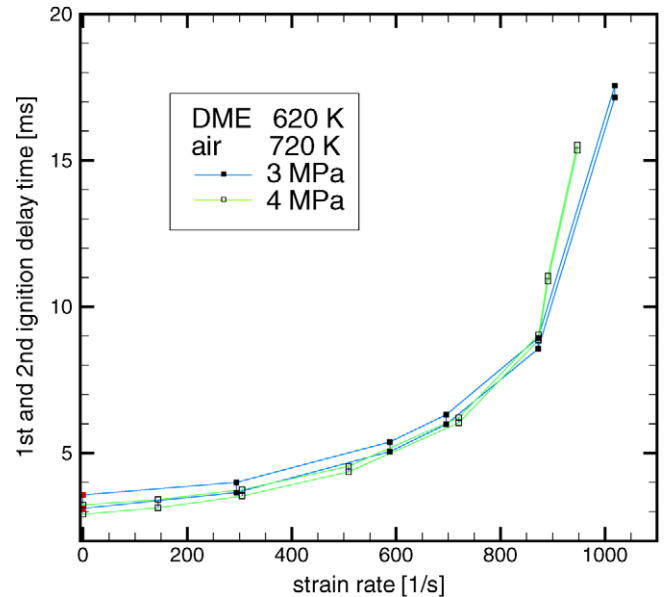


Fig. 24. The influence of flow strain on ignition delay time for 3 MPa and 4 MPa ($T_{\text{DME}} = 620$ K, $T_{\text{air}} = 720$ K). Paired points indicate first and second ignition delay time.

4 MPa. Beyond a critical strain rate of about 1000 s^{-1} auto-ignition time is outside the duration of DME injection. The strain rate in a 3D flow field is described by a tensor with six independent components of velocity gradients [45]: $S_{ij} \equiv (\partial v_i / \partial x_j) + (\partial v_j / \partial x_i)$. Here, v denotes velocity and x the coordinate of directions i, j . In the present experimental configuration, only four components in the PIV laser sheet can be measured. The analysis of strain in the stationary PIV data shows that the gradient du/dy is predominant within the jet flow field. Strain rate within the jet starts with around 10000 s^{-1} near the nozzle exit and decreases downstream to under-critical values. The associated spatial location coincides with the auto-ignition region obtained in the experiments with reaction. PIV data show turbulence levels of 40% in this region. From experimental ignition times after Table 1 and simulations in Fig. 24, it can be concluded that the shortest auto-ignitions occur for $a < 300 \text{ s}^{-1}$.

7. Conclusions

Auto-ignition of gaseous open jets during transient propagation into a high-pressure atmosphere is studied experimentally and computationally. The test facility design comprises a purgeable ignition chamber that allows for air pressures up to 4 MPa and temperatures up to 770 K. Dimethyl ether is used as single component model fuel to study the low-temperature oxidation and two-stage ignition behavior. The thermodynamic state of DME at up to 7 MPa and 620 K is super-critical to ensure the gaseous fluid state after expansion to chamber pressure. Optical access enables non-intrusive measurement techniques. Ratios of injection and chamber pressures are varied to investigate different inflow conditions. So the maximum mean nozzle exit velocities are varied between 15 and 30 m/s. Initial oscillation modes and turbulence characteristics are identified with LDV measurements. The measurements are repeated for a high number of injections confirming the very high reproducibility of the injection process. During injection, the rectangular shaped radial velocity profile at the beginning shifts to a steady-state turbulent pipe velocity shape. The axis-symmetric flow becomes stationary at about 15 ms before the subsequent DME discharges. Therefore the steady-state 2D velocity field properties of the nitrogen jet are quantified by PIV. The transient DME

inflow is measured in terms of fuel molar mixture fraction by a tracer-LIF method. The non-reacting 2D measurements are taken conditionally for discrete time steps of 1 ms after start of injection. The statistical data is analyzed to obtain local PDFs for the time-frame between DME discharge and most probable auto-ignition time. The measured PDFs of the phase-coupled mixture fraction fields of transient DME propagation are unimodal distributed. In every location the instationary PDFs are very good represented by Beta functions. This will facilitate PDF modeling and validation considerably. For both velocity and mixture fraction of the non-reacting jet flow, self-similarity of radial profiles is found already for $x/d > 2$. The preceding nitrogen jet entrains air, so that mixture fraction lies within flammability limits when DME is leaving the nozzle.

When injected into the preheated air, the auto-ignition process is visualized by high-speed shadowgraphy. At a frame rate of 1 kHz the general ignition characteristics, ignition location and ignition delay times are detected for different pressure ratios. The ignitable part of the open jet reacts simultaneously over a wide spatial extension without any hot spot ignition. Variation of nozzle exit velocity has no effect on the ignition delay time. Because mixing time scales over this flow range are very fast compared to the low-temperature chemical kinetics, the chemistry is dominating the ignition process. At a higher sampling rate of 10 kHz the two-stage ignition phenomenon is revealed evidently. For the configuration with DME at 7 MPa, 620 K and air at 4 MPa, 720 K the time delay between the first and second temperature rise is 1.4 ms.

Supplementary information is gained by instationary 1D flamelet simulations with a detailed DME reaction mechanism. The results of the simulations support the experimental findings by excellent agreement to measured effective ignition delay times at same conditions. In a parametric study the influence of pressure, air and DME temperature is determined. The ignition delay times are most sensitive to air temperature variation. This explains the width of ignition delay time distribution in the experiment. The influence of flow turbulence is assessed with the application of a strain rate parameter. The ignition delay times increase with higher strain rate up to a critical value for which ignition delay time trends to infinity. PIV analysis of primary strain confirms these computed under-critical values at locations where auto-ignition is observed. The calculated time difference between first and second stage is only 0.3 ms because the simulation is performed as an adiabatic and one-dimensional system.

The combined analysis by different measurement techniques together with flamelet simulation shows very good consistency between specific findings of diverse methods. The progress of injection and auto-ignition in a turbulent flow is quantified in comprehensive two-dimensional measurements of mixture fraction, velocity, turbulence and optical density with high temporal and spatial resolution. Accurate data provide an essential database for further theoretical studies. The results contribute to the fundamental understanding and description of hydrocarbon auto-ignition in unsteady gas jet evolution under engine relevant conditions. All findings help to improve current combustion modeling, especially with PDF methods, and to design advanced combustion concepts.

In the next step the transient injection process and auto-ignition will be modeled with the formulation of instationary PDFs. The results of the PDF simulation will be validated with the experimental observations. In addition, it is planned to confirm the findings by optical measurements like LIF of selected radicals. Future work will deal with the injection of droplets to study the auto-ignition of two-phase flows, containing spray formation and evaporation. Additionally, more complex fuels and mixtures of various fuels will be addressed to study interaction effects of different chemical kinetics.

Acknowledgment

The authors thank the DFG for financial support within the Collaborative Research Center (CRC) 606 at the Karlsruhe Institute of Technology (KIT).

Supplementary data

The online version of this article contains additional supplementary data.

Please visit DOI: [10.1016/j.combustflame.2008.07.015](https://doi.org/10.1016/j.combustflame.2008.07.015).

References

- [1] S. Fischer, F. Dryer, H. Curran, *Int. J. Chem. Kinet.* 32 (12) (2000) 713–740.
- [2] H. Curran, S. Fischer, F. Dryer, *Int. J. Chem. Kinet.* 32 (12) (2000) 741–759.
- [3] R. Bilger, S. Pope, K. Bray, J. Driscoll, *Proc. Combust. Inst.* 30 (2004) 21–42.
- [4] M. Pilling, *Low-Temperature Combustion and Autoignition*, vol. 35, Elsevier Science B.V., Amsterdam, 1997.
- [5] H. Ciezki, G. Adomeit, *Combust. Flame* 93 (1993) 421–433.
- [6] W. Gardiner, *Combustion Chemistry*, Springer-Verlag, New York, 1984.
- [7] U. Maas, J. Warnatz, *Combust. Flame* 74 (1988) 53–69.
- [8] E. Mastorakos, T. Baritaud, T. Poinot, *Combust. Flame* 109 (1997) 198–223.
- [9] R. Stauch, S. Lipp, U. Maas, *Combust. Flame* 145 (2006) 533–542.
- [10] C.N. Markides, G. De Paola, E. Mastorakos, *Exp. Therm. Fluid Sci.* 31 (2007) 393–401.
- [11] G. Jomaas, X. Zheng, D. Zhu, C. Law, *Proc. Combust. Inst.* 30 (2004) 193–200.
- [12] S. Pope, *Prog. Energy Combust. Sci.* 11 (1985) 119–192.
- [13] K. Xiao, D. Schmidt, U. Maas, *Proc. Combust. Inst.* 27 (1998) 1073–1080.
- [14] V. Saxena, B. Pope, *Combust. Flame* 117 (1999) 340–350.
- [15] A. Masri, R. Dibble, *Proc. Combust. Inst.* 22 (1988) 607–618.
- [16] R. Barlow, J. Frank, *Proc. Combust. Inst.* 27 (1998) 1087–1095.
- [17] G. Bruneaux, A study of mixture formation in direct injection diesel like conditions using quantitative fuel concentration visualizations in a gaseous fuel jet, *Society of Automotive Engineers*, Paper 2002-01-1632.
- [18] S. Sorenson, *J. Eng. Gas Turbines Power* 123 (2001) 652–658.
- [19] C. Arcoumanis, C. Bae, R. Crookes, E. Kinoshita, *Fuel* 87 (7) (2008) 1014–1030.
- [20] M. Naito, C. Radcliffe, Y. Wada, T. Hoshino, X. Liu, M. Arai, M. Tamura, *J. Loss Prevention Proc. Ind.* (Selected Papers Presented at the International Conference on Bhopal Gas Tragedy and Its Effects on Process Safety) 18 (2005) 469–473.
- [21] C. Daly, J. Simmie, J. Würmel, N. Djeballi-Chaumeix, C. Paillard, *Combust. Flame* 125 (2001) 1329–1340.
- [22] H. Curran, W. Pitz, C. Westbrook, P. Dagaut, J.-C. Boettner, M. Cathonnet, *Int. J. Chem. Kinet.* 30 (3) (1998) 229–241.
- [23] P. Dagaut, C. Daly, J. Simmie, M. Cathonnet, *Proc. Combust. Inst.* 27 (1998) 361–369.
- [24] U. Pfahl, K. Fieweger, G. Adomeit, *Proc. Combust. Inst.* 26 (1996) 781–789.
- [25] G. Fast, *Laseroptische Strömungsdiagnostik zu Selbstzündungsprozessen bei Freistrahlen*, FZKA 7288, Forschungszentrum Karlsruhe (2007), <http://bibliothek.fzk.de/zb/berichte/FZKA7288.pdf>.
- [26] B. Schneider, *Experimentelle Untersuchungen zur Spraystruktur in transienten, verdampfenden und nicht verdampfenden Brennstoffstrahlen unter Hochdruck*, Dissertation, ETH Zürich (2003).
- [27] C.J. Chen, W. Rodi, *Vertical turbulent buoyant jets: A review of experimental data*, NASA STI/Recon Technical Report A 80.
- [28] J. Zierep, *Grundzüge der Strömungslehre*, Springer-Verlag, Berlin, 1997.
- [29] K.T. Christensen, *Exp. Fluids* 36 (2004) 484–497.
- [30] D. Spalding, *Chem. Eng. Sci.* 26 (1971) 95–107.
- [31] M. Thurber, *Acetone laser-induced fluorescence for temperature and multiparameter imaging in gaseous flows*, Topical report tsd-120, Department of Mechanical Engineering, Stanford University (1999).
- [32] C. Schulz, V. Sick, *Prog. Energy Combust. Sci.* 31 (2005) 75–121.
- [33] F. Grossmann, P. Monkhouse, M. Ridder, V. Sick, J. Wolfrum, *Appl. Phys. B: Lasers Optics* 62 (3) (1996) 249–253.
- [34] Ö. Andersson, H. Neij, J. Bood, B. Axelsson, M. Alden, *Combust. Sci. Technol.* 137 (1998) 299–322.
- [35] G. Fast, D. Kuhn, *Konzentrationsmessung mittels Tracer-PLIF im instationären Dimethylether-Gasfreistrahler unter Selbstzündbedingungen*, in: *Lasermethoden in der Strömungsmesstechnik*, 14. Fachtagung, Deutsche Gesellschaft für Laser-Anemometrie GALA e.V., 2006, pp. 33.1–33.10.
- [36] J. Warnatz, U. Maas, R.W. Dibble, *Combustion*, third ed., Springer, Heidelberg, 2001.
- [37] R. Günther, *Verbrennung und Feuerung*, Springer-Verlag, Berlin, 1984.

- [38] K. Lakshminarasimhan, M. Ryan, N. Clemens, O. Ezekoye, *Proc. Combust. Inst.* 31 (2007) 1617–1624.
- [39] J. Richardson, H. Howard, R. Smith, *Proc. Combust. Inst.* 4 (1953) 814.
- [40] C. Law, *Proc. Combust. Inst.* 22 (1988) 1381–1402.
- [41] G. Stahl, J. Warnatz, *Combust. Flame* 85 (1991) 285–299.
- [42] H. Pitsch, E. Riesmeier, N. Peters, *Combust. Sci. Technol.* 158 (2000) 389–406.
- [43] L. Shiling, J. Hewson, J. Chen, *Combust. Flame* 145 (2006) 730–739.
- [44] G. Stahl, *Rechnerische Simulation stationärer und instationärer gestreckter Methan- und Propan-Luft Flammen unter Verwendung detaillierter Reaktionsmechanismen*, Dissertation, Ruprecht-Karls-Universität Heidelberg (1989).
- [45] J. Mullin, W. Dahm, *Phys. Fluids* 18 (2006) 035102.